

Personalization of Cardiac Fiber Orientations from Image Data Using the Unscented Kalman Filter

Andreas Nagler¹, Cristóbal Bertoglio¹, Michael Gee², and Wolfgang Wall¹

¹ Institute for Computational Mechanics, Technische Universität München, Germany

² Mechanics & High Performance Computing Group, Technische Universität München, Germany

Abstract. In this work, we propose to estimate rule-based myocardial fiber model (RBM) parameters from measured image data, with the goal of personalizing the fiber architecture for cardiac simulations. We first describe the RBM, which is based on a space-dependent angle distribution on the heart surface and then extended to the whole domain through an harmonic lifting of the fiber vectors. We then present a static Unscented Kalman Filter which we use for estimating the degrees of freedom of the fiber model. We illustrate the methodology using noisy synthetic data on a real heart geometry, as well as real DT-MRI-derived fiber data. We also show the impact of different fiber distributions on cardiac contraction simulations.

1 Introduction

In the last decades several studies about the cardiac fiber nature were made by performing dissections on mammalian hearts and inspecting the extracted tissue [1–4], concluding that in the human heart the fiber direction varies across the wall from about -60° to -70° in the epicardium to 60° to 70° in the endocardium regarding the circumferential direction.

These experimental observations have been classically translated into mathematical models for describing the fibers field, the so-called *rule-based models* (RBM). They mainly consist in given fiber directions on the epi- and endocardial surfaces and then interpolated inwards the heart domain by using surface distance functions (see, e.g., [5, 6]) or harmonic liftings [7, 8] in order to define the fiber vectors in the whole myocardium. RBMs have been extensively used in several works dealing with beating heart simulations (see, e.g., [9–12]).

Alternatively, *Diffusion Tensor Magnetic Resonance Imaging* (DT-MRI) allow observing the fiber structure non-invasively [13] and has been shown to be able to represent the fiber organization of the heart [14, 15]. Unfortunately, a full three-dimensional reliable acquisition and reconstruction of the fiber data through DT-MRI requires extremely long times, and therefore it can only be applied to *ex-vivo* heart samples [16–18]. Moreover, DT-MRI data is usually very noisy, in particular close to heart surface, and many uncertainties are added to the data during the segmentation, registration and postprocessing. Hence, the

direct usage of DT-MRI into, e.g., cardiac mechanics simulations, results in a nonsmooth, unphysiological stress field, making the computational model finally unreliable.

Recently, *in vivo* DT-MRI techniques were reported (see, e.g., [19] and references therein) allowing, however, only to acquire the fiber information just along some slices. Hence, a three-dimensional reconstruction of the DT-MRI data is required and further assumptions about the fiber structure and ventricular geometry are necessary [20].

The aforementioned facts motivate the methodology presented in this work for bridging RBMs and DT-MRI by fitting the model parameters from the image data, with the aim to truly personalize the myocardial architecture for patient-specific cardiac electromechanical simulations. The methodology is based on the estimation, through solving an inverse problem, the degrees-of-freedom of a RBM (namely the parameters of the angle distribution on the epi- and endocardial surfaces) from data coming, e.g., from DT-MRI, using a static Unscented Kalman Filter.

The rest of the paper is organized as follows. Section 2 describes the RBM. Section 3 presents the Unscented Kalman Filter algorithm. Section 4 shows several numerical examples. First, we test the fiber estimation scheme using noisy synthetic data. Then, numerical examples for some contraction simulations with fibers obtained through a classical RBM, fibers directly derived from DT-MRI and a RBM fibers calibrated from DT-MRI using the ROUKF are presented. Finally, we give then some conclusions and perspectives in Section 5.

2 The Fiber Model

We now summarize the RBM proposed. It is inspired from [7] and its creation consists mainly of two substeps: (a) deriving fiber values at the surfaces, and (b) domain interpolation via solving a Poisson equation.

Lets denote the computational domain of the heart as Ω , and define the surface $\Gamma \subseteq \partial\Omega$, with $\Gamma \stackrel{\text{def}}{=} S_1 \cup \dots S_n$, and \mathbf{n}_Ω the normal vector to $\partial\Omega$. In our context, S_i are subdivisions of the epi- and endocardium. Defining also the usual *long-axis* vector $\boldsymbol{\ell}$, namely the normal vector to the plane estimated from the heart base, we proceed as follows: For given degrees of freedom $\Theta = [\theta_{i,\ell}]$, $i = 1, \dots, n$, $\ell = 0, \dots, p$, with p the given order of the global angle polynomial, do

1. For each surface S_i , $i = 1 \dots n$, do
 - (a) Identify the point $\mathbf{x}_{a,i} \in S_i$ closest to the apex and find the last node $\mathbf{x}_{b,i} \in S_i$ in direction $\boldsymbol{\ell}$ starting from $\mathbf{x}_{a,i}$. Define the normalized distance function $\xi_i : S_i \mapsto [0, 1]$ such that

$$\xi_i(\mathbf{x}) = \|\mathbf{x} - \mathbf{x}_{a,i}\| / \|\mathbf{x}_{b,i} - \mathbf{x}_{a,i}\|, \quad \mathbf{x} \in S_i.$$

- (b) For a given order p , define the angle field as $\phi_i : [0, 1] \mapsto [0, \pi]$ such that

$$\phi_i(\xi_i) = \sum_{\ell=0}^p \beta_\ell \xi_i^\ell \tag{1}$$

with the coefficients β_k computed such that

$$\phi_i(\ell/p) = \theta_{i,\ell}.$$

- (c) For each node $\mathbf{x}_j \in S_i$ do
- i. Compute nodal pseudo-normal \mathbf{n}_j
 - ii. Compute circumferential direction $\mathbf{c}_j = \text{cross}(\lambda_j \mathbf{n}_j, \boldsymbol{\ell})$ with

$$\lambda_j = \begin{cases} +1 & \text{for } \mathbf{x}_j \text{ on epicardium} \\ -1 & \text{for } \mathbf{x}_j \text{ on endocardium} \end{cases}$$

so that the circumferential direction remains counterclockwise.

- iii. Evaluate the angle $\delta_j = \phi_i(\xi_i(\mathbf{x}_j))$ and the compute normalized fiber direction \mathbf{g}_j

$$\tilde{\mathbf{g}}_j = (\cos \delta_j) \mathbf{c}_j + (\sin \delta_j) \frac{\text{cross}(\mathbf{n}_j, \mathbf{c}_j)}{\|\text{cross}(\mathbf{n}_j, \mathbf{c}_j)\|}, \quad \mathbf{g}_j = \frac{\tilde{\mathbf{g}}_j}{\|\tilde{\mathbf{g}}_j\|}.$$

2. Reconstruct the fiber field $\mathbf{f} = \mathbf{f}(\mathbf{x})$, $\mathbf{x} \in \Omega$ by solving the harmonic lifting

$$\Delta \tilde{\mathbf{f}} = \mathbf{0} \quad \text{in } \Omega, \tag{2}$$

$$\tilde{\mathbf{f}} = \mathbf{g} \quad \text{on } \Gamma, \tag{3}$$

$$\partial_{\mathbf{n}_\Omega} \tilde{\mathbf{f}} = 0 \quad \text{on } \partial\Omega \setminus \Gamma, \tag{4}$$

and normalize $\mathbf{f} = \tilde{\mathbf{f}}/\|\tilde{\mathbf{f}}\|$.

3 Fiber Angles Estimation Algorithm

In practice, the degrees of freedom Θ are uncertain, but we also have access to (noisy) measurements of the fiber directions \mathbf{f}_m . We aim then to reduce these uncertainties by minimizing a cost function like:

$$J(\Theta) = \|\mathbf{f}_m - \mathbf{f}(\Theta)\|_{W^{-1}}^2 + \|\Theta - \hat{\Theta}_-\|_{P^{-1}}^2,$$

where $\hat{\Theta}_-$ is a given *a priori* value and $\|\cdot\|_{W^{-1}}$ and $\|\cdot\|_{P^{-1}}$ denote the norms used to weight both terms.

The solution techniques for this nonlinear least squares problem are classically separated in two groups: variational and filtering approaches. Variational approaches minimize this cost function by an optimization algorithm, which requires the computation of the gradient of the functional and several solutions of the forward problem $\mathbf{f}(\Theta)$. Here, we consider a filtering approach, namely the Reduced-Order Unscented Kalman Filter (ROUKF) [21], inspired from [22, 23], but in its static version, which does not require any tangent operator and the realizations $\mathbf{f}(\Theta)$ are independent, so that it is highly parallelizable.

The static ROUKF algorithm can be summarized as follows. Consider the simplex sigma-points $I_k^{(i)}$, $1 \leq i \leq k+1$ (see [24, 25]), namely

$$[I_1^{(*)}] = \left(-\frac{1}{\sqrt{2\alpha}}, \frac{1}{\sqrt{2\alpha}} \right), \quad \alpha = \frac{1}{k+1},$$

$$[I_d^{(*)}] = \begin{bmatrix} & & & 0 \\ & & & \vdots \\ & [I_{d-1}^{(*)}] & & 0 \\ \frac{1}{\sqrt{\alpha d(d+1)}} & \cdots & \frac{1}{\sqrt{\alpha d(d+1)}} & \frac{-d}{\sqrt{\alpha d(d+1)}} \end{bmatrix}, 2 \leq d \leq k.$$

Then, for given values of $\hat{\Theta}_-$ and P , perform

$$C = \sqrt{P} \quad (\text{Cholesky factorization}) \quad (5)$$

$$\hat{\Theta}_-^{(i)} = \hat{\Theta}_- + C^T I_k^{(i)}, \quad 1 \leq i \leq k+1 \quad (6)$$

$$\Gamma^{(i)} = \mathbf{f}_m - \mathbf{f}(\hat{\Theta}_-^{(i)}), \quad 1 \leq i \leq k+1 \quad (7)$$

$$L^\Theta = \alpha [\hat{\Theta}_-^{(*)}] [I_k^{(*)}]^T \quad (8)$$

$$L^\Gamma = \alpha [\Gamma^{(*)}] [I_k^{(*)}]^T \quad (9)$$

$$U = \alpha [I_k^{(*)}] [I_k^{(*)}]^T + (L^\Gamma)^T W^{-1} L^\Gamma \quad (10)$$

so that the estimated degrees-of-freedom can be computed as

$$\hat{\Theta}_+ = \hat{\Theta}_- - L^\Theta U^{-1} (L^\Gamma)^T W^{-1} \alpha \sum_{i=1}^{k+1} \Gamma^{(i)} \quad (11)$$

with, e.g., $W^{-1} = \gamma_m \mathbb{I}$ and γ_m a positive scalar.

4 Numerical Experiments

4.1 Cardiac Model

The cardiac geometry used in this study was created from high-resolution, ECG-triggered Computer-Tomography (CT) data. All four chambers were segmented using MIMICS (Materialise, Leuven, Belgium). Then, a finite element mesh of about 2.3 million tetrahedral elements, with 1.5 and 0.8 million elements for ventricles and atrias, respectively, was produced using Gmsh [26]. Here, several surfaces for the ventricles were defined for the later usage in the RBM framework, see Figure 1.

4.2 Estimation of Fiber Distributions from Synthetic and Real Data

Now we present some estimation results of the degrees-of-freedom of the fiber model presented in Section 2. We consider a reference fiber distribution for the subdivision of Γ described in Figure 1, with a linear variation of the surface fiber angle (i.e., $p = 1$), see values ‘‘Ref.’’ in Table 1.

We applied the static ROUKF procedure to estimate the RBM degrees-of-freedom from the data generated with the reference fiber distribution, perturbed

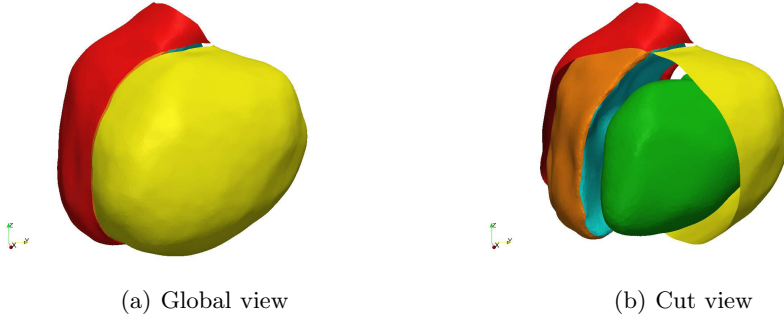


Fig. 1. Division of the surfaces of the ventricular geometry: left epicardium (yellow, S_1), right epicardium (red, S_2), left endocardium (green, S_4), right endocardium part 1 (cyan, S_3), right endocardium part 2 (orange, S_5)

by a gaussian noise with zero mean and standard deviation σ at each vector component, and finally normalized (see Figure 2). We give as an initial guess $\hat{\mathcal{X}}_-$ a constant value of 50° , an initial covariance of $P = 10^2 \mathbb{I}$, namely a standard deviation of 10° , and a weight $\gamma_m = 0.01^2$ chosen large enough so that the results are not sensitive to this value. The estimation results are summarized in Table 1. Note that even in the presence of an important amount of noise, the fiber distribution is satisfactory recovered.

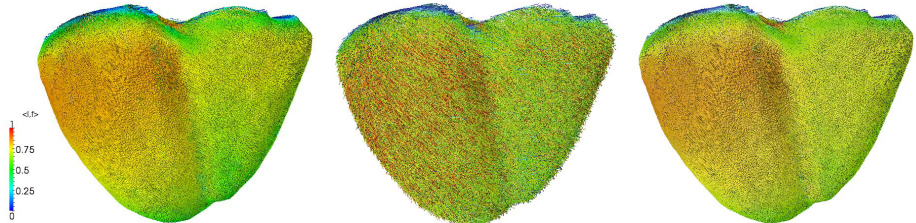


Fig. 2. Fiber distributions for reference $\sigma = 0$ (left), $\sigma = 0.2$ (center) and estimated from $\sigma = 0.2$ (right), colored by the scalar product with long axis

4.3 Estimation from DT-MRI Data and Contraction Simulations

The aim of this section is to illustrate the contraction patterns arising from different fiber organizations, in order to highlight its relevance for biophysical cardiac modeling. Within the nonlinear solid mechanics framework, we induce an active contraction in the ventricles through a classical (additive) active stress formulation [9–12] of time and space dependent magnitude (in MKS) of $2 \cdot 10^5$.

Table 1. Results of the estimation of the fiber model degrees-of-freedom from noisy synthetic data for different levels of noise

	$\hat{\theta}_{1,0}$	$\hat{\theta}_{1,1}$	$\hat{\theta}_{2,0}$	$\hat{\theta}_{2,1}$	$\hat{\theta}_{3,0}$	$\hat{\theta}_{3,1}$	$\hat{\theta}_{4,0}$	$\hat{\theta}_{4,1}$	$\hat{\theta}_{5,0}$	$\hat{\theta}_{5,1}$
Ref.	39	62	39	53	42	52	54	60	42	50
$\sigma = 0$	38.83	62.72	41.06	52.53	42.25	52.11	44.96	60.60	42.75	49.76
$\sigma = 0.1$	39.10	62.46	42.29	52.12	42.72	51.91	45.19	60.28	43.69	49.39
$\sigma = 0.2$	39.99	61.67	45.92	50.99	44.02	51.30	45.70	59.49	46.23	48.50

$\cdot f(t - \frac{\|\mathbf{x} - \mathbf{x}_{apex}\|}{0.5})$, with $f(\tau) = (0.5 \tanh(\tau) + 0.5) \tanh(10\tau) \exp(-0.5\tau^{10})$ chosen to emulate typical active stress curves, see, e.g., [27]. The passive response of the extra-fiber matrix is modeled with a nearly incompressible, hyperelastic, neo-hookean material with stiffness 20 kPa and bulk modulus 10^4 kPa . Moreover, we do not restrict any part of the boundary in order to highlight the effect of the fiber orientations in the contraction pattern. We consider then three families of fiber architectures, see Figure 3-top:

- **Model 1:** A constant angle of 60° , i.e., $p=0$ in Equation (1), with $\theta_{i,0} = 60^\circ$ on the endocardium and $\theta_{i,0} = -60^\circ$ on the epicardium.
- **Model 2:** DT-MRI derived fibers¹ registered to the CT-derived geometry.
- **Model 3:** A fiber field obtained from the ROUKF procedure using the DT-MRI data and RBM with a linear variation of the angle in the long-axis direction as in Section 4.2, i.e.: $\hat{\theta}_{1,0} = -32.3^\circ, \hat{\theta}_{1,1} = -35.7^\circ, \hat{\theta}_{2,0} = -92.7^\circ, \hat{\theta}_{2,1} = -30.8^\circ, \hat{\theta}_{3,0} = -109.7^\circ, \hat{\theta}_{3,1} = -59.0^\circ, \hat{\theta}_{4,0} = 66.6^\circ, \hat{\theta}_{4,1} = 61.7^\circ, \hat{\theta}_{5,0} = 71.1^\circ, \hat{\theta}_{5,1} = 19.6^\circ$.

The results for the contraction simulation are shown in Figure 3. Please note first that, as mentioned in the introduction, the resulting stress distribution with Model 2 is non-smooth and with unphysiological stress peaks, in opposite to Models 1 and 3. Also the dynamics of the heart differs substantially with the different fiber models. In Models 2 and 3 the apex moves mainly parallel to the short-axis staying close to its original position, something that can actually also be observed *in-vivo*. In contrast, in Model 1 the apex moves towards the base. To the authors best knowledge, the constant fiber angle distribution like in Model 1 is actually the most used approach in current cardiac simulation practice, which “obligates” modelers to fix the apex in order to obtain more physiological contraction dynamics, see, e.g., [10, 11]. Let us also remark that the estimated fibers (Model 2) are in good agreement with DT-MRI data in the left ventricle, so that for this region the contraction pattern is similar for both Models 2 and 3. However, in the right ventricle there is still an important mismatch between Model 2 and 3 (in both fibers and contraction), probably due to the fact that the chosen RBM is not detailed enough to reproduce such a fiber pattern, which encourages the development of more general RBMs.

¹ Openly available on http://gforge.icm.jhu.edu/gf/project/dtmri_data_sets/

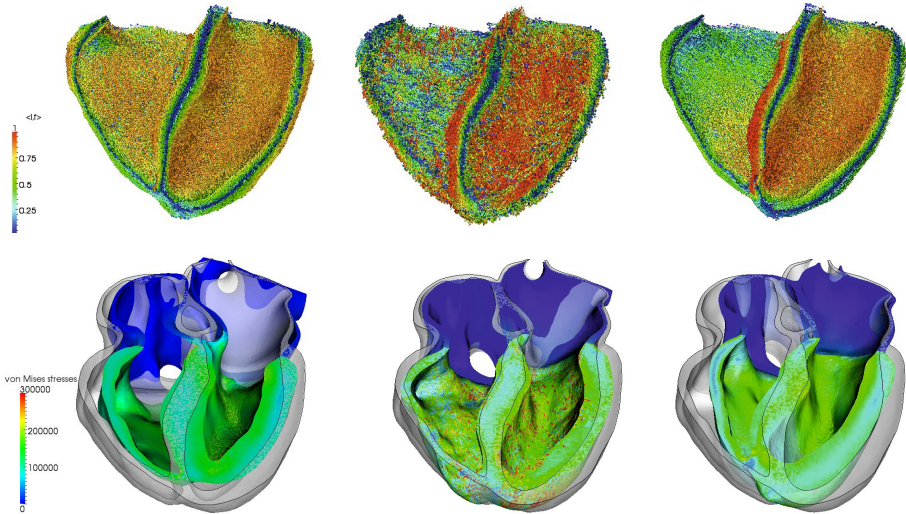


Fig. 3. Top: Short-axis view of the ventricular fiber organization, colored by the magnitude of long-axis component. Bottom: Snapshots of the contraction simulation at time 0.3 s, superposed with the original geometry (grey). From left to right: Models 1 to 3.

5 Conclusions and Perspectives

We introduced a methodology for estimating the degrees-of-freedom of a Ruled Based Model (RBM) for cardiac fiber architecture from DT-MRI data. We first detailed the mathematical fiber RBM. Then, we outlined the estimation algorithm, namely a reduced-order Unscented Kalman Filter (ROUKF), in order to minimize the discrepancy between measured and model fiber distribution by optimizing the degrees-of-freedom of the RBM. Next, we showed some estimation results from noisy synthetic data, emulating DT-MRI. Finally, we presented fiber estimation results with real DT-MRI data and we illustrated the impact of different fiber organizations in cardiac contraction simulations. Ongoing work involves: (a) the improvement of the RBM based, e.g., on the observations reported in [18] in order to better match more realistic fiber architectures, and (b) the estimation of the RBM degrees-of-freedom from multi-slice DT-MRI data.

Acknowledgements. The results presented in this article are part of the *Advanced Cardiac Mechanics Emulator*, an initiative supported by the Institute for Advanced Study (TU München) and one of its fellow Prof. Michael Ortiz (Caltech), whom we sincerely thank.

References

1. Streeter, D.D., Spotnitz, H.M., Patel, D.P., Ross, J., Sonnenblick, E.H.: Fiber orientation in the canine left ventricle during diastole and systole. *Circulation Research* 24(3), 339–347 (1969)

2. Armour, J., Randall, W.: Structural basis for cardiac function. *American Journal of Physiology – Legacy Content* 218(6), 1517–1523 (1970)
3. Greenbaum, R.A., Ho, S.Y., Gibson, D.G., Becker, A.E., Anderson, R.H.: Left ventricular fibre architecture in man. *British Heart Journal* 45(3), 248–263 (1981)
4. LeGrice, I.J., Smaill, B.H., Chai, L.Z., Edgar, S.G., Gavin, J.B., Hunter, P.J.: Laminar structure of the heart: ventricular myocyte arrangement and connective tissue architecture in the dog. *American Journal of Physiology - Heart and Circulatory Physiology* 269(2), H571–H582 (1995)
5. Potse, M., Dube, B., Richer, J., Vinet, A., Gulrajani, R.: A comparison of monodomain and bidomain reaction-diffusion models for action potential propagation in the human heart. *IEEE Trans. Biomed. Eng.* 53, 2425–2435 (2006)
6. Chapelle, D., Fernández, M.A., Gerbeau, J.-F., Moireau, P., Sainte-Marie, J., Zemzemi, N.: Numerical simulation of the electromechanical activity of the heart. In: Ayache, N., Delingette, H., Sermesant, M. (eds.) *FIMH 2009*. LNCS, vol. 5528, pp. 357–365. Springer, Heidelberg (2009)
7. Wong, J., Kuhl, E.: Generating fibre orientation maps in human heart models using poisson interpolation. *Computer Methods in Biomechanics and Biomedical Engineering*, 1–10, PMID: 23210529 (2012)
8. Bayer, J., Blake, R., Plank, G., Trayanova, N.: A novel rule-based algorithm for assigning myocardial fiber orientation to computational heart models. *Annals of Biomedical Engineering* 40, 2243–2254 (2012)
9. Goektepe, S., Kuhl, E.: Electromechanics of the heart: a unified approach to the strongly coupled excitation contraction problem. *Computational Mechanics* 45, 227–243 (2010)
10. Chabiniok, R., Moireau, P., Lesault, P.F., Rahmouni, A., Deux, J.F., Chapelle, D.: Estimation of tissue contractility from cardiac cine-mri using a biomechanical heart model. *Biomechanics and Modeling in Mechanobiology*, 1–22 (2011), doi:10.1007/s10237-011-0337-8
11. Xi, J., Lamata, P., Niederer, S., Land, S., Shi, W., Zhuang, X., Ourselin, S., Duckett, S.G., Shetty, A.K., Rinaldi, C.A., Rueckert, D., Razavi, R., Smith, N.P.: The estimation of patient-specific cardiac diastolic functions from clinical measurements. *Medical Image Analysis* (2012)
12. Lafortune, P., Ars, R., Vázquez, M., Houzeaux, G.: Coupled electromechanical model of the heart: Parallel finite element formulation. *International Journal for Numerical Methods in Biomedical Engineering* 28(1), 72–86 (2012)
13. Basser, P., Mattiello, J., Lebihan, D.: Estimation of the effective self-diffusion tensor from the nmr spin echo. *Journal of Magnetic Resonance, Series B* 103(3), 247–254 (1994)
14. Hsu, E.W., Muzikant, A.L., Matulevicius, S.A., Penland, R.C., Henriquez, C.S.: Magnetic resonance myocardial fiber-orientation mapping with direct histological correlation. *American Journal of Physiology - Heart and Circulatory Physiology* 274(5), H1627–H1634 (1998)
15. Scollan, D.F., Holmes, A., Winslow, R., Forder, J.: Histological validation of myocardial microstructure obtained from diffusion tensor magnetic resonance imaging. *American Journal of Physiology - Heart and Circulatory Physiology* 275(6), H2308–H2318 (1998)
16. Helm, P., Beg, M.F., Miller, M.I., Winslow, R.L.: Measuring and mapping cardiac fiber and laminar architecture using diffusion tensor MR imaging. *Annals of the New York Academy of Sciences* 1047(1), 296–307 (2005)

17. Helm, P.A., Tseng, H.J., Younes, L., McVeigh, E.R., Winslow, R.L.: Ex vivo 3D diffusion tensor imaging and quantification of cardiac laminar structure. *Magnetic Resonance in Medicine* 54(4), 850–859 (2005)
18. Lombaert, H., Peyrat, J., Croisille, P., Rapacchi, S., Fanton, L., Cheriet, F., Clarysse, P., Magnin, I., Delingette, H., Ayache, N.: Human atlas of the cardiac fiber architecture: study on a healthy population. *IEEE Transactions on Medical Imaging* 31(7), 1436–1447 (2012)
19. Gamper, U., Boesiger, P., Kozerke, S.: Diffusion imaging of the in vivo heart using spin echoes considerations on bulk motion sensitivity. *Magnetic Resonance in Medicine* 57(2), 331–337 (2007)
20. Toussaint, N., Sermesant, M., Stoeck, C.T., Kozerke, S., Batchelor, P.G.: *in vivo* human 3D cardiac fibre architecture: Reconstruction using curvilinear interpolation of diffusion tensor images. In: Jiang, T., Navab, N., Pluim, J.P.W., Viergever, M.A. (eds.) MICCAI 2010, Part I. LNCS, vol. 6361, pp. 418–425. Springer, Heidelberg (2010)
21. Moireau, P., Chapelle, D.: Reduced-order Unscented Kalman Filtering with application to parameter identification in large-dimensional systems. *COCV* 17, 380–405 (2011), doi:10.1051/cocv/2010006
22. Julier, S., Uhlmann, J., Durrant-Whyte, H.: A new approach for filtering nonlinear systems. In: American Control Conference, pp. 1628–1632 (1995)
23. Julier, S., Uhlmann, J., Durrant-Whyte, H.: A new method for the nonlinear transformation of means and covariances in filters and estimators. *IEEE Transactions on Automatic Control* 45(3), 477–482 (2000)
24. Pham, D.-T., Verron, J., Gourdeau, L.: Filtres de Kalman singuliers évolutifs pour l'assimilation de données en océanographie. *Comptes Rendus de l'Académie des Sciences - Series IIA* 326(4), 255–260 (1998)
25. Hoteit, I., Pham, D.-T., Blum, J.: A simplified reduced order Kalman filtering and application to altimetric data assimilation in Tropical Pacific. *Journal of Marine Systems* 36(1–2), 101–127 (2002)
26. Geuzaine, C., Remacle, J.F.: Gmsh: A 3-d finite element mesh generator with built-in pre- and post-processing facilities. *International Journal for Numerical Methods in Engineering* 79(11), 1309–1331 (2009)
27. Sainte-Marie, J., Chapelle, D., Cimrman, R., Sorine, M.: Modeling and estimation of the cardiac electromechanical activity. *Computers & Structures* 84(28), 1743–1759 (2006)